Performance of turbulence closure models for 3D RANS simulation of urban flooding with exchanges between flooded streets and building openings

Shuyue Yu[(1,2)], Xuefang Li[(1)]*, Vasileios Kitsikoudis[(3)], Guilhem Dellinger[(4)], Lihua Chen[(1)], Chengguang Lai[(1,5)], Léo Guiot[(4)], Sébastien Erpicum[(2)], Benjamin Dewals[(2)]

[(1)] College of Civil Engineering and Architecture, Guangxi University, Nanning, China

[(2)] Hydraulics in Environmental and Civil Engineering (HECE), University of Liège (ULiège), Belgium

[(3)] Water Engineering and Management, University of Twente, Enschede, The Netherlands

[(4)] ICube laboratory, National school for water and environmental engineering, Strasbourg, France

[(5)] School of Civil Engineering and Transportation, South China University of Technology

*Corresponding authors: Xuefang Li (lxuefangcn@gxu.edu.cn; xuefang.li@uliege.be)

ABSTRACT

Urban flooding poses significant risks to densely populated areas, necessitating accurate predictive models for effective risk management. While 3D computational fluid dynamics (CFD) models are increasingly used to simulate flood dynamics, the selection of an appropriate turbulence closure model remains critical yet underexplored in the context of urban flooding. This study evaluates the performance of three widely used Reynolds-Averaged Navier-Stokes (RANS) turbulence models: standard k-ε, k-ω, and k-ω SST, in simulating urban flooding in an idealized urban district model with flow intrusion into buildings. Based on laboratory experiments reported in the literature, we conducted three-dimensional simulations using OpenFOAM. Nine urban configurations were considered, each with different opening layouts that allow flow intrusion into buildings. The discharge distribution, surface flow patterns, and velocity fields at selected cross-sections were analyzed. Results show that the simulated discharge partitions match the measured values closely and lie within the ±1.5% uncertainty of the experimental data with all three tested turbulence closures, demonstrating the reliability of the numerical approach. In terms of surface flow and velocity characteristics, the k-ε and k-ω SST models showed better agreement with experimental observations than the k-ω model, particularly in capturing complex surface structures, internal recirculation zones, and along-stream velocity variations. This study provides insights into turbulence model selection for urban flood simulations, particularly those involving flow intrusion into buildings. It constitutes a useful reference for future urban flood modeling.

Keywords: Urban flooding; Flow structure; Turbulence closure model; 3D modelling

1 Introduction

The frequency and intensity of extreme urban flooding events have increased due to rapid urbanization and more frequent extreme rainfall events associated with climate change (Wang et al., 2023; Tang et al., 2024; Fang, 2016; Hettiarachchi et al., 2018). Such events can cause significant economic losses and even lead to a high number of fatalities (Kreibich et al., 2019), which makes flood risk prediction and management a key urban management priority (Guo et al., 2021; Luo et al., 2022; Rosenzweig et al., 2021). However, predicting urban flooding is a major challenge because of the high variability of flow patterns resulting from the intricacy of urban environments (Li et al., 2025; Saleem et al., 2025), and the multitude of features that interact with the flow, such as sewer systems, buildings, underground spaces, and the flood storage capacity within urban blocks (Kitsikoudis et al., 2021; Mejía-Morales et al., 2023; Mignot et al., 2019; Wu et al., 2024; Yuan et al., 2024). Flood risk is generally assessed based on flow characteristics such as flow depth, flow velocity, and flood duration at local scales (Xia et al., 2014; Zhu et al., 2023). Therefore, advancing our understanding of urban flood processes and accurately quantifying the flow characteristics within urban areas is of utmost importance (Beteille, 2024; Dewals et al., 2023).

To thoroughly investigate the hydraulic characteristics of urban flooding, in addition to collecting field data (Chanson et al., 2018), laboratory experiments designed for different urban configurations have also provided valuable insights (Dong et al., 2021; Finaud-Guyot et al., 2019; Li et al., 2022; Mejía-Morales et al., 2023; Mignot et al., 2019; Sañudo et al., 2024). These experimental datasets offer reliable references for the development and validation of numerical models, allowing urban flood hydraulics to be explored in greater depth through numerical simulations (Dellinger et al., 2025; Dewals et al., 2023; Li et al., 2025; Wu et al., 2024). Two-dimensional models are more commonly used to reproduce urban flood processes, whereas the application of 3D models to urban flooding has only emerged in recent years (Li et al., 2025; Viccione et al., 2022; Zhu et al., 2023). Two-dimensional models that solve the depth-averaged shallow water equations, offer high computational efficiency and have

demonstrated good agreement with experimental results for flow depth and discharge partitioning in urban networks (Dewals et al., 2023; Liang et al., 2024; Luo et al., 2018). However, the depth-averaged formulation restricts the ability of 2D models to resolve vertical flow structures and complex three-dimensional flow patterns (Haider et al., 2024; Li et al., 2024). Similar limitations associated with simplified flow representations have also been reported in studies comparing reduced-dimensional and three-dimensional simulations. For example, Luo et al. (2018) showed in a comparative 1D–3D numerical study of open-channel junction flows that simplified models tend to underestimate energy losses and secondary circulations, highlighting the importance of resolving three-dimensional flow structures in junction-dominated flows. Likewise, Ouro et al. (2024) compared several computational hydraulics models ranging from depth-averaged shallow-water formulations to fully three-dimensional approaches. They reported that three-dimensional models generally provide more accurate predictions of mean velocities and flow dynamics in open-channel flows with lateral cavities.

To address the limitations of conventional depth-averaged models in representing vertical flow structures and complex three-dimensional flow patterns, several improved depth-integrated models have been proposed to incorporate key three-dimensional flow effects into two-dimensional frameworks. For example, Blanckaert et al. (2003) developed a nonlinear model to account for the redistribution of mean flow and secondary currents in curved open-channel flows. Uchida et al. (2019) further proposed a two-phase depth-integrated approach capable of reproducing non-hydrostatic effects. More recently, Castro-Orgaz et al. (2025) and Lugina et al. (2026) proposed enhanced depth-integrated formulations based on additional equations of motion accounting for non-uniform velocity vertical profile and non-hydrostatic pressure distribution, which are excluded in the conventional 2D model. These developments illustrate the ongoing effort to bridge the gap between computationally efficient depth-averaged models and fully three-dimensional simulations.

In recent years, refined three-dimensional computational fluid dynamics (CFD) models have been increasingly applied to urban flood simulations. For instance, Zhu et al. (2023) analyzed the influence of urban neighborhood layouts on flow intrusion into residential buildings and on pedestrian safety, showing that 3D simulations can effectively capture flood exchanges between buildings and streets under various urban configurations. In urban flooding, strong three-dimensional flow separation, reattachment, and vortex formation occur around buildings and street junctions, and 3D numerical simulations enable a more realistic representation of these hydraulic structures and improve the understanding of local flow dynamics (Finaud-Guyot et al., 2019; Li et al., 2025). Li et al. (2024) compared a depth-averaged k-ε 2D model with a 3D Reynolds-Averaged Navier–Stokes (RANS) model using the k-ω SST closure in a study of urban flood modelling with different urban layouts, but no flow intrusion within buildings nor urban blocks. Their results indicated that the 2D model can provide reasonable predictions of overall flood dynamics and water levels, making it suitable for large-scale flood propagation analyses. However, the 3D model reproduced more accurately jet trajectories and complex recirculation patterns that cannot be resolved by depth-averaged approaches. Li et al. (2025) further extended this modelling comparison to configurations involving exchanges between flooded streets and building interiors. Their results showed that the 3D model reproduces more accurately the shape and size of recirculation zones and captures vertical velocity variations associated with jet flows, while the 2D depth-averaged model exhibited systematic limitations. In particular, the 2D model failed to reproduce the water level fluctuations observed in the experiments, showed larger errors in the prediction of discharge partitioning among outlets, and produced distorted recirculation structures compared with the measurements. These results highlight the limitations of depth-averaged approaches for representing complex three-dimensional flow structures in urban flooding. Moreover, these results imply that while depth-averaged models may be efficient for large-scale flood propagation, they can be inadequate when complex three-dimensional flow structures, such as jets, recirculations, and vertical velocity variations, play an important role. Viccione et al. (2022) used a 3D CFD model based on RANS equations coupled with a k–ε turbulence model to simulate flood–building

interactions, showing that local flow kinematics strongly affect flood forces acting on building facades and demonstrating the capability of 3D models to assess these effects. Dellinger et al. (2025) evaluated 2D models (with and without the k–ε closure) and a 3D k–ω SST model against experimental data for urban flood flows in a realistic street network. They showed that the 3D model effectively reproduced the recirculation behind intersections. Recently, Saleem et al. (2025) simulated dam-break-induced urban flooding using a 3D CFD model, revealing that while grid refinement reduces numerical errors, the selection of an appropriate turbulence closure is the primary factor in capturing high-inertia flow dynamics. Their sensitivity analysis of RANS-based models demonstrates that the realizable k–ε variant significantly outperforms the standard k–ε and other closures, achieving high predictive accuracy (NSE > 0.75) and superior computational efficiency in complex urban geometries.

These studies demonstrate the value of 3D turbulence models for urban flood simulations. However, the reliability of such simulations depends strongly on the turbulence closure used, as previous studies have shown that different RANS turbulence models can lead to significant differences in predicted flow fields. For example, Farhadi et al. (2018) compared the performance of the standard k-ε, the classical k-ω and an improved k-ω model incorporating a cross-diffusion term and a modified stress limiter in three-dimensional racetrack flume experiments, showing that these turbulence closure methods did not exhibit significant differences in capturing the overall flow structures. Shaheed et al. (2019) compared the performance of the standard k-ε model and the realizable k-ε model in curved and confluent channels, showing that the standard k-ε model captures better velocity profiles in curved channels, while the realizable k-ε model was more accurate in confluent channels. This indicates that the performance of turbulence closures can depend strongly on the flow geometry.

Table 1 provides a summary of previous numerical studies employing turbulence closure models to investigate the detailed flow characteristics of urban environments and selected examples of open-channel flows. The table lists the type of numerical model (2D or 3D), the turbulence closure adopted, the model configuration, and whether the study considered urban

flooding or included a comparative analysis. This overview highlights the limited number of comparative studies focusing on urban flooding, particularly regarding flow intrusion into buildings or urban blocks.

Overall, several studies based on 3D RANS turbulence models have produced insightful results that have advanced our understanding of urban flooding processes. Likewise, comparative analyses have been conducted to evaluate different turbulence closures for open-channel flow conditions. However, evaluations focusing specifically on turbulence closures for urban flooding, particularly those involving flow exchanges between building interiors and the surrounding streets, remain limited. Thus, information that can help selecting turbulence models in such configurations is scarce.

The present study aims to evaluate the performance of turbulence closure models in 3D RANS simulations of urban flooding within an idealized district with flow intrusion into buildings. By systematically comparing the standard k-ε, k- ω, and k-ω SST models, the study seeks to clarify their relative strengths and limitations in predicting urban flow variables. Special attention is paid to the representation of near-wall effects and flow mixing at bifurcations and junctions, which are critical to capturing flow patterns in urban environments and assessing the flood hazard. The work of Mejía-Morales et al. (2021) offers a valuable reference, as their experiments on an idealized urban district with different openings around an urban block provide representative configurations for model validation. Building upon recent research (Dewals et al., 2023; Li et al., 2025), this study further analyses the ability of three turbulence closures to reproduce complex flow patterns resulting from street-building interactions during urban flooding, across nine geometric configurations.

Section 2 briefly introduces the experimental setup of Mejía-Morales et al. (2021), the tested urban configurations, and the computational framework with the selected turbulence models. Sections 3 and 4 present the simulation results and discussion, respectively, while Section 5 summarizes the main conclusions.

Table 1 Previous numerical research with turbulence closures on detailed flow characteristics in open channels/urban area.

Reference	Model (2D or 3D)	Turbulence Closure	Model Configurations	Urban Flooding Scenarios	Comparative Studies of Turbulence Closure
Luo et al. (2018)	3D	k–ω SST	Junction	No	No
Farhadi et al. (2018)	3D	k–ε and k–ω	Racetrack flumes	No	Yes
Shaheed et al. (2019)	3D	k–ε and k–ω	Curved and confluent channels	No	Yes
Viccione et al. (2022)	3D	k–ε	Urban basin	Yes	No
Zhu et al. (2023)	3D	k–ε	Grid of building blocks	Yes	No
Saleem et al. (2025)	3D	k–ε	Grid of building blocks	Yes	No
Li et al. (2024)	3D	k–ω SST	District	Yes	No
Li et al. (2025)	3D	k–ω SST	District	Yes	No
Dellinger et al. (2025)	2D and 3D	k–ω SST	District	Yes	No
Current study	3D	k–ε, k–ω and k–ω SST	District	Yes	Yes

2 Methodology

2.1 Experimental setup

This study is based on experimental research on urban flooding at a city block scale conducted by Mejía-Morales et al. (2021). The physical model represents a rectangular urban block surrounded by four streets as depicted in Figure 1(a). Openings in the central block enable flow exchanges between the streets and the interior of the block, with the aim of representing the intrusion of water into buildings through open or broken doors during an urban flood. All streets had a uniform rectangular cross-section with a width of 0.15 m. The x-direction had a slope of

0.12%, while the *y*-direction remained flat. The dimensions of the central urban block were 1.56 m × 0.96 m. The central block was delimited by walls with a thickness of 2 cm and a height of 15 cm.

In the experimental model, two inlets, Inlet 1 and Inlet 2, were positioned at the upstream end of the *x*-direction. Inlet 1 had a consistent inflow rate of 4.5×10^{-3} m^3/s, while the Inlet 2 flow rate was set at 2×10^{-3} m^3/s. Four outlets were placed at the ends of the four street sections, with vertical weirs enabling adjustment of the water depth. Outlet 1 featured a weir measuring 4 cm in height, whereas the remaining three outlets were equipped with weirs measuring 3 cm in height. The measurement methods are explained in detail in Mejía-Morales et al. (2021).

Experimental measurements of key hydraulic variables, including water depth, flow velocity, and discharge, were conducted for a series of urban-block configurations with different numbers and positions of openings Mejía-Morales (2022). From these configurations, nine representative cases were selected for the present study (Figure 1b). For clarity and simplicity, these configurations are renamed sequentially as configurations A, B, C, D, E, F, G, H, and I.

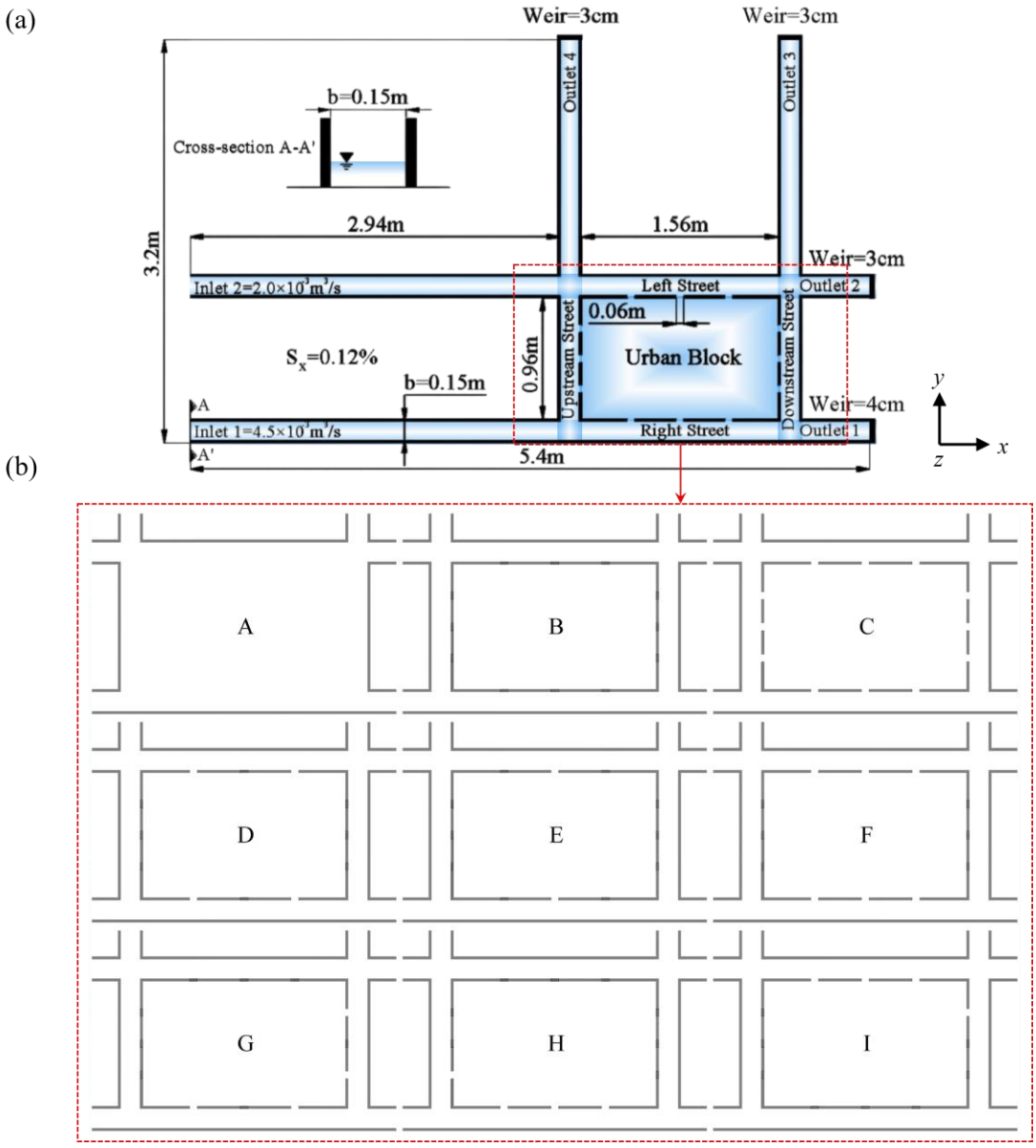

Figure 1 Details of the modeling approach. (a) Top view of the experimental setup of Mejía-Morales et al. (2021). (b) The nine block configurations selected for numerical modeling, obtained by closing different combinations of openings.

2.2 3D Numerical modelling

Model description

The experimental model was reproduced by solving numerically the 3D incompressible RANS equations in OpenFOAM (v9). The adopted solver is interFoam, which is primarily used for two-phase incompressible and turbulent flows. A structured mesh is chosen to build the computational domain (Figure 2).

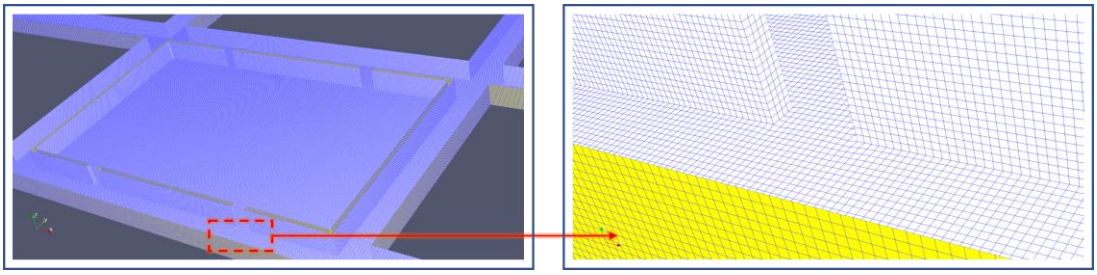

Figure 2 Model grid structure (using Configuration D as an example).

The free surface was captured with the volume of fluid (VOF) method introduced by Hirt et al. (1981). This method is computationally efficient, it is one of the most used methods to predict free surface flows and has been extensively validated (Torres et al., 2022). Cells containing only water or only air are assigned values of $\alpha_{water} = 1$ and $\alpha_{water} = 0$, respectively. The free surface is identified at locations where $\alpha_{water} = 0.5$. A Courant-Friedrichs-Lewy (i.e., CFL) restriction of 1 was imposed, which led to an adaptive time step of the order of 0.002 s.

In this study, three two-equation Reynolds-averaged turbulence closures available in OpenFOAM, namely the standard *k*-ε (Farhadi et al., 2018), *k*-ω (Wilcox, 2008), and *k*-ω SST models (Li et al., 2025), were selected for the simulations. These models were considered appropriate because they are widely used in hydraulic engineering and free-surface turbulent flow simulations, while remaining computationally affordable for three-dimensional computations involving multiple configurations. Compared with higher-fidelity approaches such as large-eddy simulation (LES), they offer a more practical balance between computational cost and predictive capability. In addition, these three turbulence closures are among the most used models in engineering CFD and therefore provide a representative basis for assessing the influence of turbulence-model selection on simulated urban flood structures. The Wilcox *k*-ω formulation and its later developments have also played an important role in the evolution of widely used RANS turbulence closures. In the following, these models are referred to as *k*-ε, *k*-ω, and *k*-ω SST, respectively.

Boundary conditions

The models require consideration of three distinct boundary condition types: inlet, outlet, and solid wall boundaries (Figure 1a). At the beginning of each simulation, the water inside the domain was initialized as a stagnant layer with a uniform depth of 5 cm.

a) Inlet

The inlet boundary conditions are prescribed to reproduce the experimental inflow conditions. The inflow section corresponds to the experimental inlet configuration, with an opening height of 4 cm. The velocity at the inlet is specified to match the experimental discharge, ensuring that the inflow rate in the simulations is consistent with the experimental conditions. This configuration reproduces the subcritical flow regime observed in the experiments. Turbulence quantities at the inlet are prescribed as constant values following standard RANS practice, including the turbulent kinetic energy k and the second turbulence variable required by each turbulence model, i.e., the turbulent kinetic energy dissipation rate, ε, or the specific dissipation rate, ω.

b) Outlet

A free-outflow boundary condition is prescribed at the outlet. It includes zero-gradient treatment for the water phase fraction and constant atmospheric pressure for the free surface.

c) Solid wall boundaries

At solid boundaries, all three turbulence models use wall-function approaches to treat turbulent kinetic energy, turbulent viscosity, and dissipation rates. These treatments provide constraints on turbulence production and dissipation at walls, which are essential for accurately representing near-wall turbulence in both low- and high-Reynolds number flows. Because the laboratory experiment was built with smooth plexiglasses, the walls are treated as hydraulically smooth in the simulations.

Simulation convergence

To evaluate the convergence of the numerical models, a trial simulation was conducted using the *k-ω* SST model with a mesh size of 5 mm for Configuration H. The hydrographs at the four outlets and Coefficient of variation (C_V) of outflow discharge at different time periods are shown in Figure 3 (b). C_V here was calculated as the ratio of the standard deviation to the mean value of the each outlet discharge. It is used to describe the variability in time of the flow variables. After about 50 s, the discharge exhibited quasi-steady behavior, with the value of mean C_V dropping from 2.44×10^{-1} to 7.36×10^{-3}.

During the simulation period of 50 to 100 seconds, the C_V of discharge exhibits a steady small value compared to the period of 0 to 50 seconds. Based on these observations, the time-averaged values after 50 seconds (from 50 s to 100 s) are used in this study as the reference for steady-state analysis.

Simulations ran in parallel using the public domain OpenMPI implementation of standard MPI on the high-performance computing platform of Guangxi University, with the Sugon 7000A supercomputer as the core.

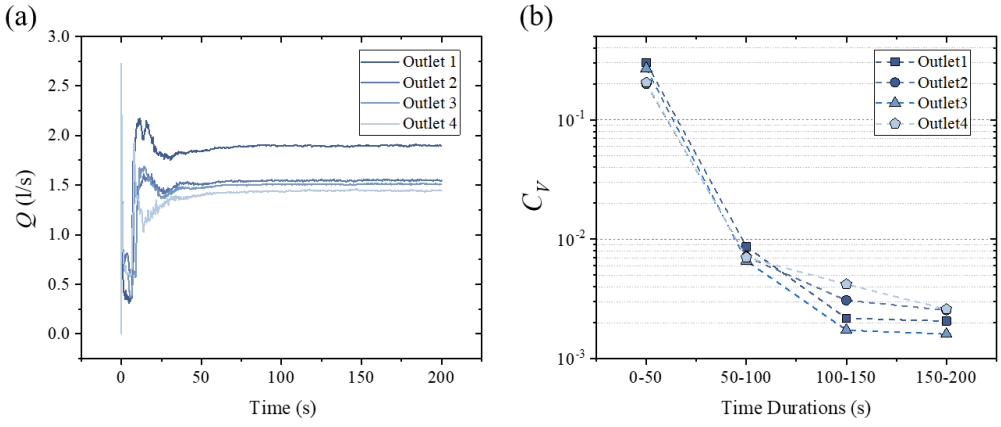

Figure 3 (a) Outflow discharge hydrograph of numerical simulation. (b) Coefficient of variation (C_V) of outflow discharge at different time periods (taking Configuration H with the *k-ω* SST turbulence model and a mesh resolution of 5 mm as an example)

3 Results

3.1 Grid independence test

Mesh sensitivity tests are conducted for Configuration H using uniform hexahedral meshes with three cell sizes of d = 4 mm, 5 mm, and 10 mm. All the other modelling parameters were kept the same. The total number of mesh cells is 6.5×10^6 (4mm), 3.3×10^6 (5mm) and 0.4×10^6 (10mm).

Mesh independence is assessed by comparing both the discharge partitioning and the flow patterns across the domain. The volumetric flow rate through the outlet patches is calculated based on the VOF method as:

$$\dot{V}_{water} = \sum_{f \in surface} \phi_f \cdot \alpha_{water,f} \quad (1)$$

where $\dot{V}_{water}$ is the volumetric flow rate of water (m³/s), ϕ_f is the volumetric flux across face f (m³/s), and $\alpha_{water,f}$ is the volume fraction of water at face f.

Figure 4 presents the discharge partition at the four outlets and under the three mesh resolutions for each turbulence model. The results indicate good mesh convergence for all three turbulence models. Variations in discharge distribution caused by changes in mesh resolution are generally small, with average differences below 1.5%. The largest difference occurs at Outlet 1 between the 4 mm and 5 mm meshes using the *k-ω* model (2.16%).

The influence of mesh resolution on simulated surface flow patterns is shown in Figure 5. For the *k-ε* and *k-ω* SST models, surface flow characteristics such as velocity field, flow contractions and separations, and recirculation locations appear not significantly affected by mesh resolution. For the *k-ω* model, flow velocity and overall patterns are also relatively insensitive to mesh resolution in most regions. However, the flow pattern inside the block varies substantially. Velocity magnitudes predicted by the *k-ω* model under all three mesh resolutions are lower than those from the other two models. Moreover, with a 4 mm mesh, large recirculations inside the building barely form, whereas in the 5 mm and 10 mm cases, recirculations develop clearly. This indicates that the *k-ω* model's prediction of internal

building flow is more sensitive to mesh resolution than the other two models. This behavior is consistent with the known characteristics of the classical *k-ω* formulation, which can be more responsive to changes away from solid boundaries (Menter, 1994) and may therefore contribute to the variations observed here. Considering the mesh sensitivity results and computational efficiency, a mesh size of 5 mm is chosen to be used for all subsequent simulations.

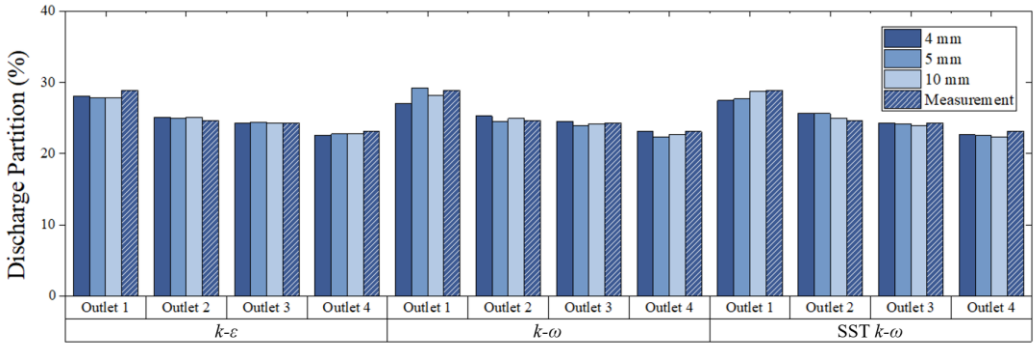

Figure 4 Outflow discharge distribution at the four outlets for measurements and numerical modeling with different mesh resolutions (4 mm, 5 mm, and 10 mm) for three turbulence closure models. The values represent the time-averaged proportion of each outlet discharge relative to the total outflow, based on the converged results from each simulation.

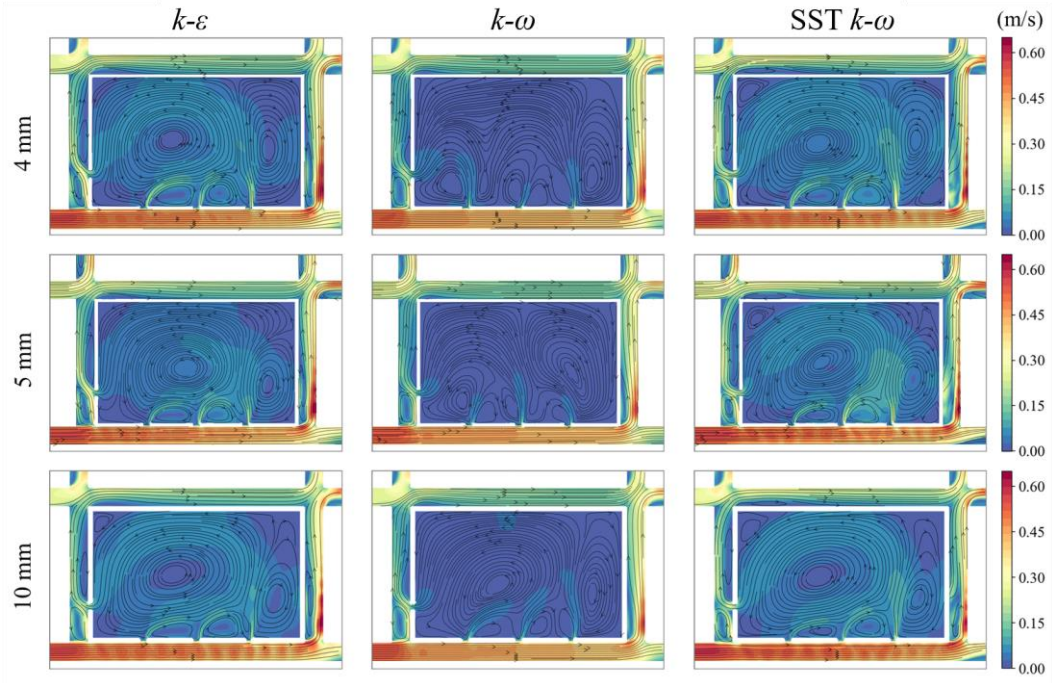

Figure 5 Surface flow velocity patterns from three turbulence models at different mesh resolutions. The figures show the surface layer data, with streamlines overlaid on velocity contour maps, with Figure 9 providing the measured surface flow pattern.

3.2 Discharge partition

Figure 6 shows the discharge partition in the experiments and simulations. The error bars represent the experimental measurement uncertainty (1.5% according to Mejía-Morales et al., 2021) and the standard deviation of the simulated discharge ratios after convergence.

In Configurations B–I, Outlet 1 consistently receives the largest share of the total outflow, Outlets 2 and 3 have similar proportions, and Outlet 4 receives the least. All simulations capture these trends reasonably well, although the k–ε model shows discrepancies in Configurations D and H. Indeed, as shown in Figure 7, most simulated discharge fractions fall within the ±1.5% experimental uncertainty when compared to the respective measurements. For Configurations B–I, the k-ω model matches the experimental measurements most closely, while the k-ε and k-ω SST models consistently underestimate the discharge in Outlet 1.

Configuration A, by contrast, behaves differently due to the absence of guiding streets. In this configuration, the k–ω model does not reproduce the correct ranking, and both the k–ε and k–ω SST models show a larger standard deviation than k–ω, with particularly pronounced variations at Outlet 1 for the k–ω SST model. In general, the k–ε and k–ω SST models exhibit larger temporal variations than the k–ω model across Configurations B–I, and these differences become more pronounced in Configuration A.

After convergence of the simulations, the standard deviation of the time series of computed discharge fractions ranges from 0.001% to 1.149%, with the k–ω SST model generally associated with the highest level of temporal variability among the tested closures.

In several configurations, the root means square errors (RMSE) (Figure 8) indicate that the k–ω model generally performs particularly well, with RMSE values below 0.5 in all cases except Configuration A. In comparison, the k–ε and k–ω SST models remain valuable alternatives, with the k–ε model performing better than k–ω SST in an open geometric configuration such as Configuration A.

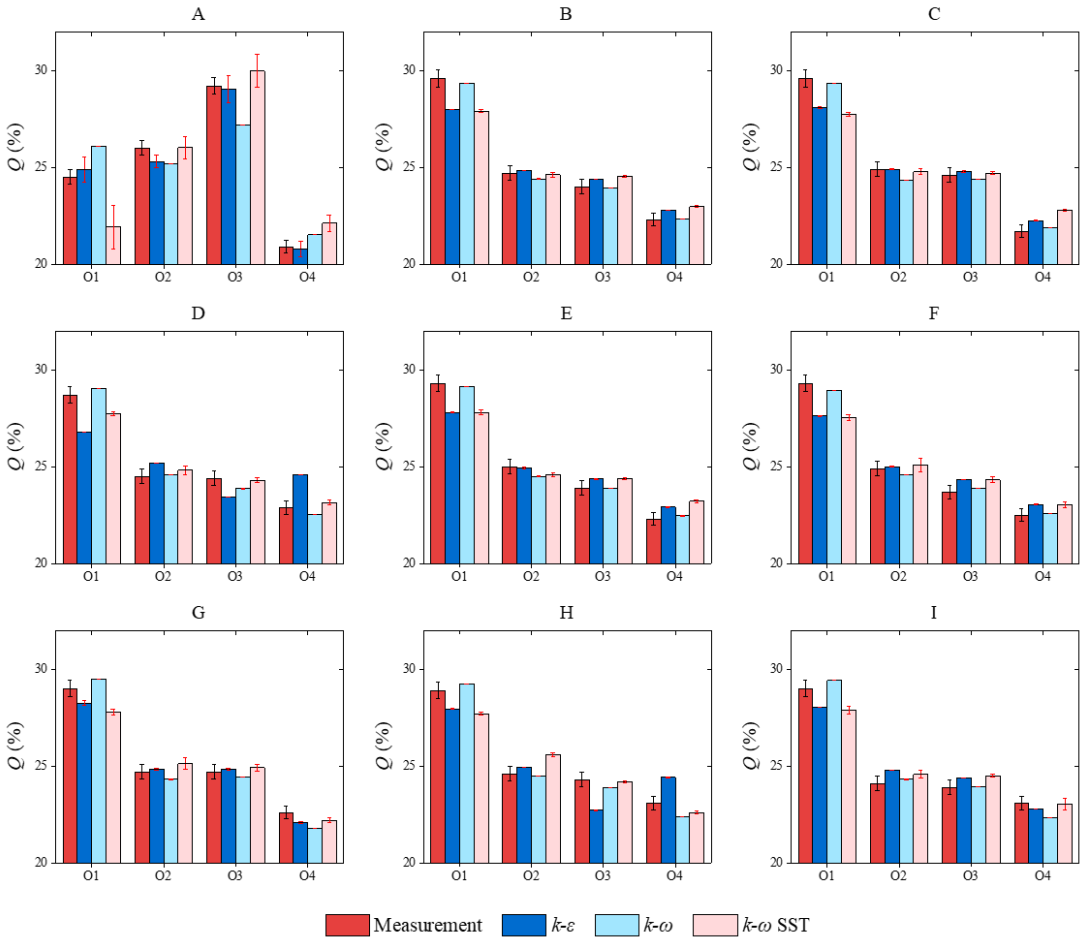

Figure 6 Measured and modelled discharge partitions by the three turbulence models at the four outlets for all configurations (A - I). O1–O4 denote Outlets 1 to 4. The error bars represent the measurement uncertainty associated with the experimental instrumentation (Mejía Morales, 2022) and sample standard deviation for simulations.

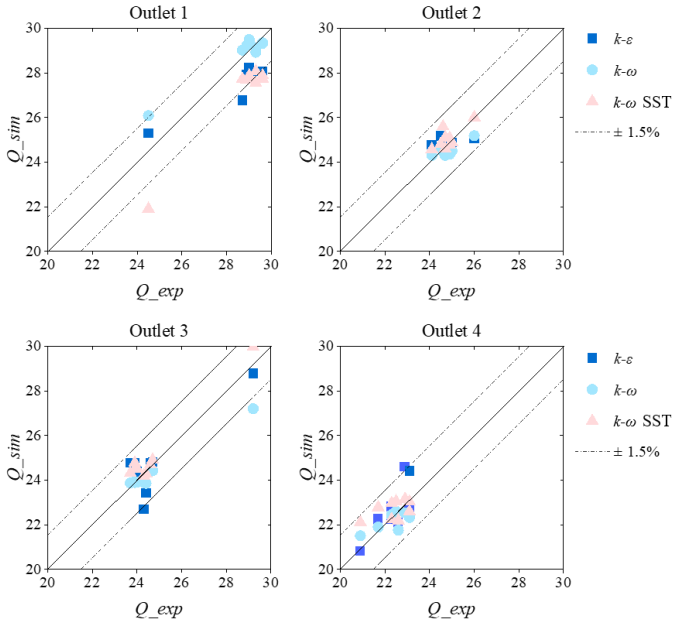

Figure 7 Comparison of discharge partition at the four outlets between physical experiments (x-axis) and 3D CFD simulations (y-axis) for the three tested turbulence closures and all the studied cases (Figure 1b). Each subplot corresponds to one outlet, showing the percentage of total outflow through that outlet.

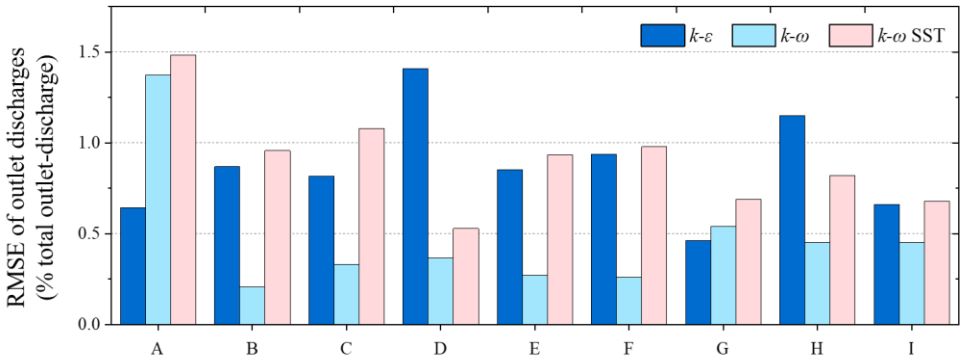

Figure 8 RMSE between three turbulence models simulations and measured outlet discharges at the four outlets. The RMSE is calculated based on the discharge portion in each outlet relative to the total outflow.

3.3 Surface velocity

Flow patterns within the streets

Figure 9 shows the time-averaged surface flow patterns. Results are presented for the measurements and for the three turbulence models. In the Right street of the physical model, all configurations exhibit a general decrease in flow velocity from upstream to downstream. This trend is also reproduced in numerical simulations. The *k-ε* and *k-ω* SST models successfully capture the superimposed along-stream fluctuations observed in the measurements, whereas the *k-ω* model tends to under-represent these fluctuations, showing instead a more uniform, monotonic velocity decline. These differences are further illustrated in Figure 10 which presents the time-averaged surface velocity profiles along the centerline of the Right street for both the measurements and the three turbulence models. Configuration A is not included, as it does not contain the Right street. The *k-ε* and *k-ω* SST models reproduce satisfactorily the general trend of the measured data. The magnitude of the fluctuations is generally higher in the *k–ω* SST results than in the *k–ε* results and is closer to the fluctuation level measured in the experiments, as seen in Configurations B, C, F, H, and I. In some cases, such as Configuration D, the two models show nearly identical fluctuation levels, while in

Configuration E, it is difficult to determine which model aligns more closely with the measurements.

Although the k-ω model fails to reproduce these local fluctuations in the Right street in most configurations, its overall trend in flow velocity variation remains reasonably consistent with the measurements.

While Figure 10 highlights the model performance along the Right street, Figure 9 further illustrates differences in the simulated surface flow patterns at street intersections, where all three models successfully reproduce the characteristic surface flow patterns formed by flow confluences and bifurcations. The recirculation zones along streets show distinct differences between the models. For instance, in Configuration D, the experimental flow pattern inside the Upstream street indicates that the recirculation generated from the inflow of Right street spans near half the street length. The k-ε model overestimates this zone, extending it to nearly the entire street, while the k-ω model provides the most accurate approximation. In contrast, the k-ω SST model generates a unique "8"-shaped recirculation zone, deviating significantly from both the experimental data and the other models.

Similar discrepancies in the k-ω SST model are observed in upstream streets at configurations D, E, F, G, and H. These differences extend to Downstream streets, where the flow pattern in the confluence simulated by the k-ω SST model diverges consistently from both the experimental measurements and the outputs of the other two models. A detailed analysis of these discrepancies is presented in the subsequent section on vertical flow structures.

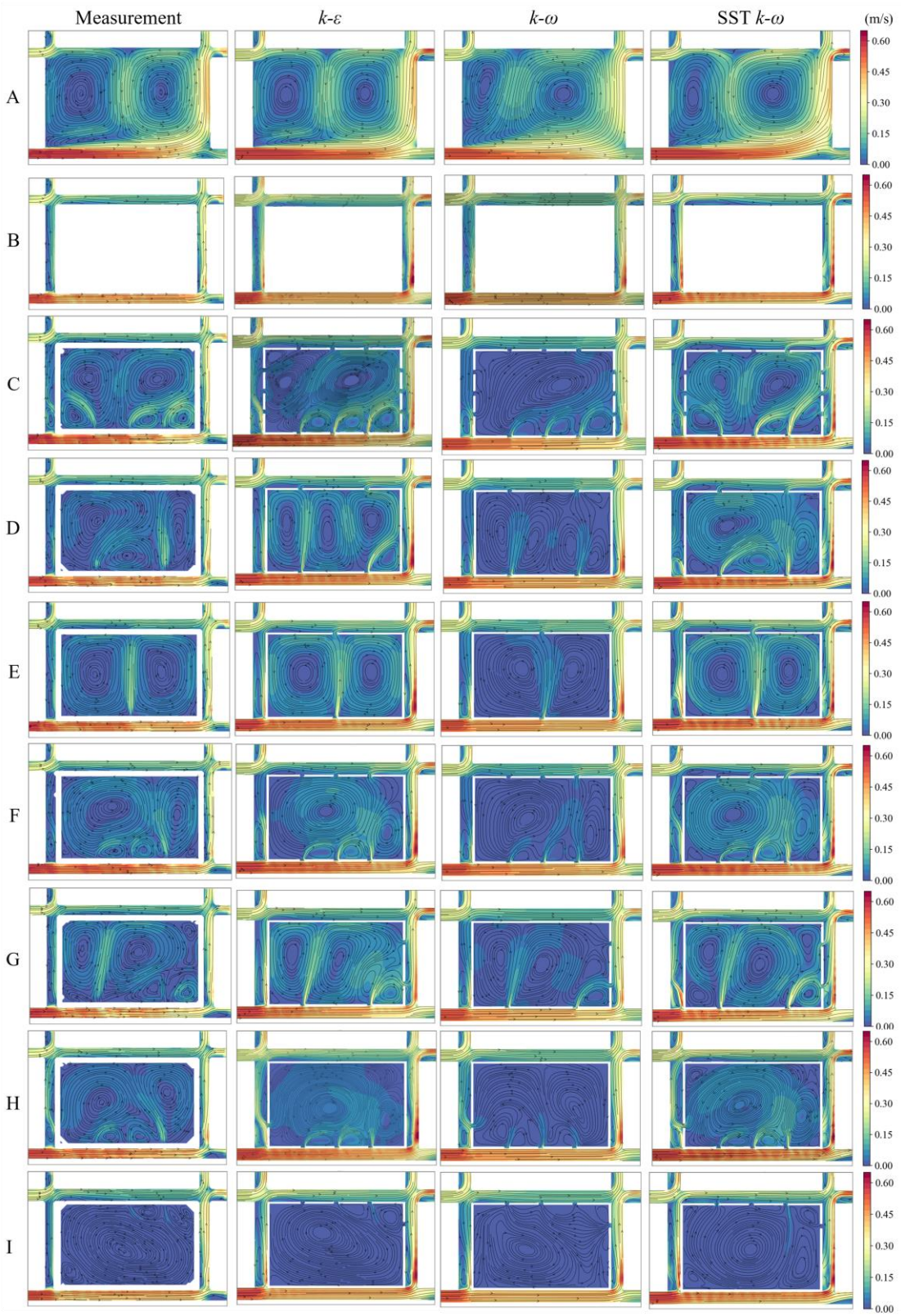

Figure 9 Time-averaged surface flow velocity patterns from measurements and those computed with the turbulence models *k*-*ε*, *k*-*ω* and *k*-*ω* SST. The color scale represents the horizontal velocity magnitude (m/s).

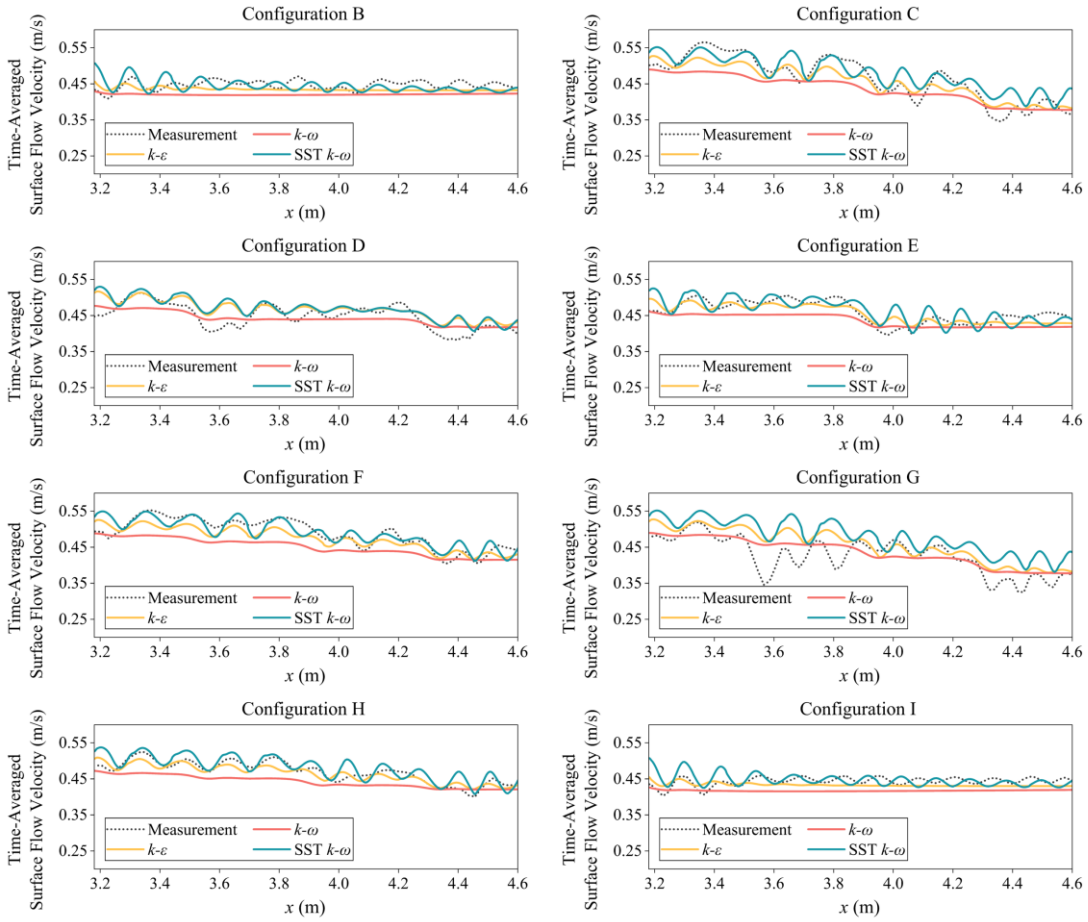

Figure 10 Time-averaged surface flow velocity profiles from measurement and three turbulence models along the centerline of Right street.

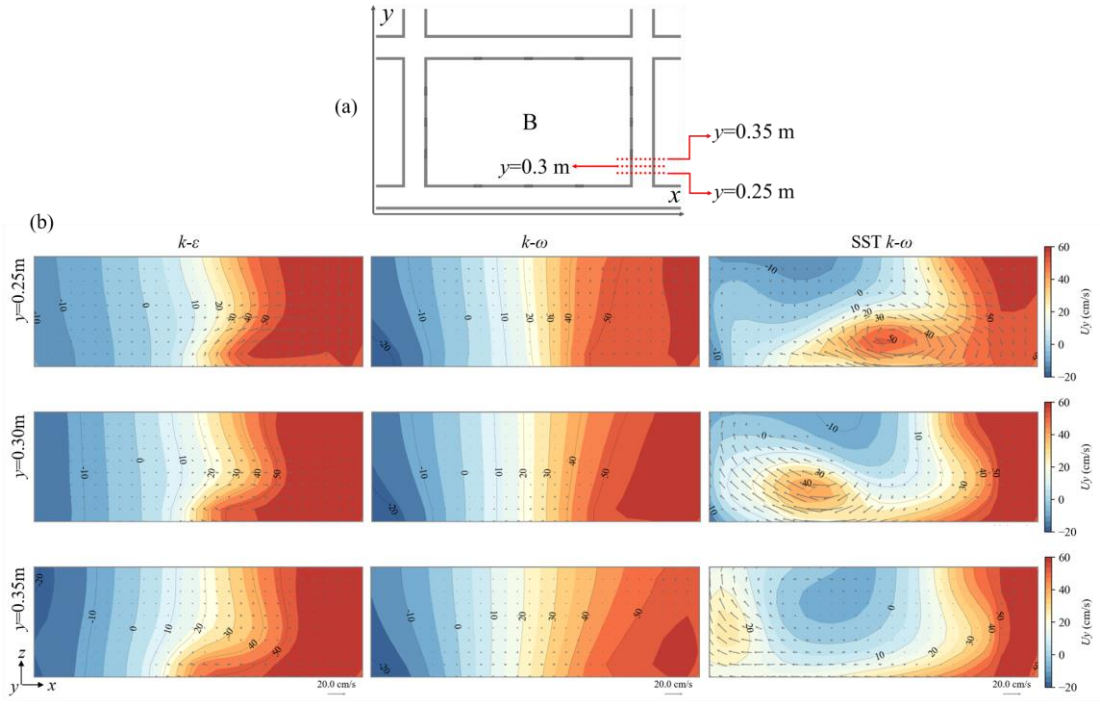

Figure 11 (a) The red dashed lines show cross-sections of y = 0.25 m, 0.30 m, and 0.35 m in the Downstream street of Configuration B. (b) Contours of U_y overlaid with quiver plots of U_x and U_z at cross-sections in three turbulence models.

Taking Configuration B as an example, Figure 11 compares the flow patterns predicted by the three turbulence models at three cross-sections (y = 0.25 m, 0.30 m, and 0.35 m) within the recirculation zone in the Downstream street formed by flow separation at the junction with the Right street. It should be noted that the experimental flow field data for these cross-sections were not recorded. In all three numerical models, each cross-section shows a flow pattern with positive U_y near the downstream side, where peak velocities exceed 60 cm/s, and negative U_y appear near the upstream side, indicating a recirculating flow structure in the vertical flow pattern. However, the detailed velocity structures vary considerably among the models. The flow field predicted by the k-ω model is structurally the simplest, featuring a clear division with positive U_y near the right side and negative U_y near the left side of the sections, and no obvious velocity layering along the z direction, indicating relatively uniform velocity distribution from the surface to the bottom. In addition, the velocity gradient is more pronounced near the bed and becomes weaker toward the free surface.

In terms of U_y contours, the k-ε model exhibits a moderately complex flow structure. In the upper half near the free surface, U_y and its gradient are similar to those predicted by the k-ω model. In the lower half near the bed, the high-velocity region adjacent to the downstream side shows a clear tendency to extend toward the upstream side, resulting in velocity variations in the vertical direction. This difference becomes even more pronounced in the simulation results of the k-ω SST model. At the cross-section located at y = 0.25 m, the downstream region displays a high-velocity positive U_y zone. Near the bottom center of the section, an elliptical high-velocity region accompanied by a recirculation zone (as indicated by the U_x and U_z quiver plot) is observed. As the flow progresses to the cross-sections at y = 0.30 m and 0.35 m, this high-speed zone shifts upstream, its magnitude gradually decreases, and the recirculation becomes weaker until it approaches the wall. Meanwhile, the area of reverse flow also shifts, moving from the upstream wall toward the free surface at the center of the section.

All three models exhibit significant spatial variability in the vertical distribution of flow velocity. The structure of the velocity variation differs markedly among the models, which is closely related to the distinct approaches each turbulence model employs in resolving near-wall flows. As shown in the velocity profiles, the k–ε model shows a wider near-wall high-speed region than the k–ω and k–ω SST models. In terms of the velocity gradient along the x-direction, however, the k–ε and k–ω models show a more comparable trend, both exhibiting a nearly linear variation.

Flow patterns within the urban block and open spaces

In addition to the flow features observed in the streets, Figure 9 also shows the flow patterns inside the model buildings. Table 2 summarizes the number and relative size of recirculation zones predicted by the different turbulence models. This qualitative comparison helps identify systematic differences in the flow structures reproduced by the turbulence closures in the idealized domain. In real cases, where the scale of the problem is different and the urban layout is considerably more complex, additional uncertainties may occur that are related to parameterizations for roughness or drag coefficients.

Configuration A features an open-space layout, where the simulated velocity distributions are generally close to the experimental observations. The k–ε model reproduced two large and nearly symmetric recirculations that closely matched the measurements. In contrast, the k–ω and k–ω SST models produced two asymmetric recirculations, with noticeable deviations in their shape and center position compared with the experiments.

The k-ε and k-ω SST models produced more accurate results, showing better agreement with the measured data for the size and location of large recirculations in most configurations. However, in some configurations, one model performed better than the other. For example, in Configuration D, the k-ε model produced significant errors, while the k-ω SST model performed well. Conversely, in Configuration I, the k-ε model yielded a better simulation, while the k-ω SST model generated slightly less accurate results.

Further differences emerged when simulating cases with smaller recirculations and local flow velocities. The k-ω SST model provided a more accurate representation of recirculation velocity in Configuration C, reproduced the right-side recirculation in Configuration F more accurately both in terms of size and extent, and captured the position of the small recirculation in Configuration G more effectively than the k-ε. In Configuration H, the results of the k-ε and the k-ω SST were almost identical, although both deviated substantially from the experimental observations.

The flow patterns predicted by the k-ω turbulence model showed noticeable discrepancies compared to the measurements, primarily due to its systematic underestimation of flow velocity. This underprediction not only reduced the strength of recirculation but also caused deviations in their location and size. In Configurations C, D, H, and I, the k-ω model results exhibited clear differences from the measurements in both velocity magnitude and flow structures, particularly in the position and extent of the recirculation centers. In Configurations E, F, and G, the k-ω model simulations reproduced the overall positioning of the recirculation reasonably well, although the predicted velocities inside the buildings remained more than 50% lower than the measured values on average.

Table 2 Qualitative appraisal of the agreement between observed and computed flow patterns within the block interior (Configurations B - H) and in a large open space (Configuration A). Notation "L" stands for "large recirculation(s)", "S" for "small recirculation(s)" and "s" for "very small recirculation(s)".

Configuration	Measurement	*k-ε*	*k-ω*	*k-ω* SST
A	2L, symmetrically	2L, symmetrically	2L, asymmetrically	2L, asymmetrically
B	-	-	-	-
C	2L+3S	2L+3L+1s, inaccurately	1L+3S, inaccurately	2L+3S
D	3L	3L+1S, inaccurately	2L+2S, inaccurately	3L
E	2L, symmetrically	2L, symmetrically	2L, symmetrically	2L, symmetrically
F	2L+2S	2L+2S	2L+2S	2L+2S
G	2L+2S+3s	2L+2L	2L+2S	2L+3S+1s
H	2L+2S	2L+2S, incorrect relative sizes	2L+3S	2L+2S+1s, incorrect relative sizes
I	1L+4S	1L+2S	1L	1L+3S

4 Discussion

Evaluating the performance of turbulence models in urban flood simulations requires balancing modeling accuracy and computational efficiency, with flow patterns serving as a key indicator of model fidelity. Under identical computational settings (grid resolution of 5 mm, about 3.3 million cells, and parallel computation with 24 cores on an Intel i9-13900 processor with DDR5 memory), the *k-ω*, *k-ω* SST, and *k-ε* models completed the 200-second simulation in approximately 212, 249, and 295 hours, respectively. Taking the average runtime of 252 hours as a reference, the *k-ω* model was about 16% faster, while the *k-ε* model required about 17% longer computational time.

Beyond runtime, numerical oscillation also influences model efficiency. An analysis of the coefficient of variation of outlet discharges revealed some systematic differences among the turbulence models, with the *k-ω* model showing the smallest fluctuations, followed by the *k-ε*

model, and the *k-ω* SST model exhibiting slightly higher variability in most cases (eight out of nine cases). In Case A, the *k-ω* SST model presented a relatively larger variation, with a standard deviation of approximately 1.14% in the discharge partition.

It is worth noting that these numerical fluctuations cannot be directly compared with the experimental results, because the experimental data used here represent time-averaged conditions rather than instantaneous flow variations. Therefore, the observed differences in numerical oscillations should be interpreted as indicators of computational robustness, not as measures of physical unsteadiness. Nevertheless, video references provided by the experimental dataset (Mejía Morales, 2022) reveal that the flow sometimes exhibits noticeable temporal variability within the flow domain despite the fact that incoming flow is steady. In particular, the flow pattern evolves over time, especially in the jet formed as the flow enters the building through the opening (see Supplementary Figure S1). This jet-induced fluctuation was also reproduced in the simulations: both the *k-ε* and *k-ω* SST models captured similar oscillatory behavior, whereas the *k-ω* model, due to its notably lower velocities inside the building, failed to reproduce this feature clearly. Although this temporal variability has not been quantitatively analyzed within the scope of the present study, its qualitative characteristics provide a valuable reference, suggesting that the experimentally observed fluctuations and the turbulence model's ability to capture such flow variability merit further investigation.

This analysis highlights that higher numerical resolution and sensitivity to transient flow features may increase computational time and introduce more variability in simulated discharge. The selection of an appropriate turbulence model should be guided by the objectives of the study, considering whether the priority lies in computational efficiency or in capturing detailed transient behaviors. Table 3 summarizes the main characteristics of each turbulence closure model.

Table 3 Summary of the main strengths and limitations of the three turbulence models applied in this study.

Turbulence model	Computational time (hours)	Strengths	Limitations	Performance in narrow streets with surface velocity fluctuations
k-ε	295	Best for open, unobstructed flows.	Long runtime, less accurate in surface flow patterns at intersections	Captures trend, less pronounced fluctuations.
k-ω	212	About 16% faster, accurate discharge	Underestimates interior flows	Smooth velocity decay, minimal fluctuations.
k-ω SST	249	Captures recirculation well	May generate spurious vortices	Consistent trend, closest match to measured fluctuations.

5 Conclusions

This study systematically evaluated the performance of three turbulence closure models: *k-ε*, *k-ω*, and *k-ω* SST, in simulating urban flooding through an idealized district with flow exchanges between streets and building openings.

Mesh sensitivity tests confirmed that the simulation results are generally mesh independent for all three turbulence models. Variations in discharge distribution across different mesh resolutions remained below 1.5%, indicating good numerical convergence. Surface flow structures, such as velocity fields and recirculation zones, were largely unaffected by mesh refinement, except for minor differences in recirculation formation within the building when using the *k-ω* model.

When compared to the respective measurements, most simulated discharge partitions at the different outlets fall within the ±1.5% experimental uncertainty. The *k-ε* and *k-ω* SST models outperformed the *k-ω* model at capturing complex flow features within building interiors and street networks, including recirculation zones, as well as contraction and expansion of flow at street intersections. In narrow street segments where surface velocity fluctuations were observed, all models reproduced the general decreasing trend in flow velocity from upstream to downstream. However, the *k-ε* and *k-ω* SST models more accurately represented

superimposed along-stream fluctuations. The *k-ω* SST model showed the closest agreement with the measurements, while the *k-ω* model tends to smooth out these variations. This makes the *k-ε* and *k-ω* SST models more suitable for assessing flood risk in streets with complicated flow patterns, and in large open spaces, such as squares and car parks.

Of the three models tested, the differences in computational efficiency remained at around 15%. The *k-ω* model required the least computational time, followed by *k-ω* SST and standard *k-ε*. No single model excelled in all aspects. The choice of turbulence model should be guided by the specific objectives of the simulation, whether prioritizing discharge accuracy, flow velocity details, or computational speed.

Future research should extend this work by incorporating more complex urban drainage systems to explore the interactions between surface flooding and sewer networks, particularly during surcharge conditions. Incorporating pollutant transport and contaminant intrusion into buildings would also enhance the applicability of the model for urban risk assessment (Han et al., 2025). Moreover, simulating the movement and accumulation of floating debris or drifters could provide new insights into flood-induced hazards, such as the impacts on building facades or other structural elements (Albano et al., 2016; Bayón et al., 2024). In addition, coupling hydrodynamic simulations with pedestrian stability and exposure analyses would allow for assessing risks faced by pedestrians during urban flood events (Arrighi et al., 2017; Zhu et al., 2023). These extensions would contribute to a more comprehensive understanding of urban flood dynamics and improve predictive capabilities for flood resilience planning.

Acknowledgements

This work was funded by the National Natural Science Foundation of China (No. 52309015) and Guangxi Specific Research Project for Research Bases and Talents (No. AD23026176). This is also funded by Guangxi Young Elite Scientist Sponsorship Program (GXYESS2025022). The support from the French National Research Agency (ANR) for the project DEUFI (ANR-18-CE01-0020) is also acknowledged

References

Albano, R., Sole, A., Mirauda, D., Adamowski, J., 2016. Modelling large floating bodies in urban area flash-floods via a Smoothed Particle Hydrodynamics model. Journal of Hydrology, 541: 344-358. DOI:https://doi.org/10.1016/j.jhydrol.2016.02.009

Arrighi, C., Oumeraci, H., Castelli, F., 2017. Hydrodynamics of pedestrians' instability in floodwaters. Hydrol. Earth Syst. Sci., 21(1): 515-531. DOI:10.5194/hess-21-515-2017

Bayón, A., Valero, D., Franca, M.J., 2024. Urban flood drifters (UFD): Identification, classification and characterisation. Journal of Flood Risk Management, 17(3): e13002. DOI:https://doi.org/10.1111/jfr3.13002

Beteille, E., 2024. Étude expérimentale des écoulements instationnaires dans les zones urbanisées. PhD thesis, École des Ponts ParisTech.

Blanckaert, K., Vriend, H.J. de, 2003. Nonlinear modeling of mean flow redistribution in curved open channels. Water Resources Research 39.

Castro-Orgaz, O., Cantero-Chinchilla, F.N., Ali, S.Z., Dey, S., 2025. Vertically averaged and moment equations for free surface flows: Pressure-Poisson solver, breaking waves, and morphodynamic modeling. Physics of Fluids 37, 125110.

Chanson, H., Brown, R., 2018. Stability of Individuals during Urban Inundations: What Should We Learn from Field Observations?, Geosciences. DOI:10.3390/geosciences8090341

Chen, Y., Zhou, H., Zhang, H., Du, G., Zhou, J., 2015. Urban flood risk warning under rapid urbanization. Environmental Research, 139: 3-10. DOI:https://doi.org/10.1016/j.envres.2015.02.028

Dellinger, G., Guiot, L., Pujol, L., Lawniczak, F., Fran, cois, P., Finaud-Guyot, P., Vazquez, J., & Garambois, P.-A. (2025). Assessing 3D and 2D hydrodynamic models for urban flood simulations: a district scale analysis with experimental street-level discharge, height and velocity. Urban Water Journal, 22(9), 1084-1102. doi:10.1080/1573062X.2025.2531460.

Dewals, B. J., Kantoush, S. A., Erpicum, S., Pirotton, M., & Schleiss, A. J. (2008). Experimental and numerical analysis of flow instabilities in rectangular shallow basins. Environmental Fluid Mechanics, 8(1), 31 – 54-31 – 54.

Dong, B., Xia, J., Zhou, M., Deng, S., Ahmadian, R., & Falconer, R. A. (2021). Experimental and numerical model studies on flash flood inundation processes over a typical urban street. Advances in Water Resources, 147, 103824-103824.

Fang, Q., 2016. Adapting Chinese cities to climate change. Science, 354(6311): 425-426. DOI:10.1126/science.aak9826

Farhadi, A., Mayrhofer, A., Tritthart, M., Glas, M., Habersack, H., 2018. Accuracy and

572 comparison of standard k-ϵ with two variants of k-ω turbulence models in fluvial
573 applications. Engineering Applications of Computational Fluid Mechanics, 12(1): 216-235.
574 DOI:10.1080/19942060.2017.1393006

575 Finaud-Guyot, P., Garambois, P.A., Dellinger, G., Lawniczak, F., François, P., 2019.
576 Experimental characterization of various scale hydraulic signatures in a flooded branched
577 street network. Urban Water Journal, 16(9): 609-624.
578 DOI:10.1080/1573062X.2020.1713173

579 Guo, K., Guan, M., Yu, D., 2021. Urban surface water flood modelling – a comprehensive
580 review of current models and future challenges. Hydrol. Earth Syst. Sci., 25(5): 2843-2860.
581 DOI:10.5194/hess-25-2843-2021

582 Haider, S., Gabriel, H.F., Yang, L., Shahid, M., Mubeen, A., 2024. Dam Break Flow: A
583 Comparative Model Study Using OpenFOAM and BASEMENT. Arabian Journal for
584 Science and Engineering, 49(4): 5385-5401. DOI:10.1007/s13369-023-08400-9

585 Han, C., Kawaike, K., Koshiba, T., Wada, K., Chen, X., & Liu, L. (2025). Integrated modeling
586 of urban flood inundation and pollutant transport considering building-scale exchanges.
587 Journal of Hydrology, 662, 133854. doi:https://doi.org/10.1016/j.jhydrol.2025.133854

588 Hettiarachchi, S., Wasko, C., Sharma, A., 2018. Increase in flood risk resulting from climate
589 change in a developed urban watershed – the role of storm temporal patterns. Hydrol. Earth
590 Syst. Sci., 22(3): 2041-2056. DOI:10.5194/hess-22-2041-2018

591 Hirt, C.W., Nichols, B.D., 1981. Volume of fluid (VOF) method for the dynamics of free
592 boundaries. Journal of Computational Physics, 39(1): 201-225. DOI:10.1016/0021-
593 9991(81)90145-5

594 Kitsikoudis, V., Erpicum, S., Rubinato, M., Shucksmith, J. D., Archambeau, P., Pirotton, M.,
595 & Dewals, B. (2021). Exchange between drainage systems and surface flows during urban
596 flooding: Quasi-steady and dynamic modelling in unsteady flow conditions. Journal of
597 Hydrology, 602, 126628. doi:https://doi.org/10.1016/j.jhydrol.2021.126628

598 Kreibich, H., Thaler, T., Glade, T., Molinari, D., 2019. Preface: Damage of natural hazards:
599 assessment and mitigation. Nat. Hazards Earth Syst. Sci., 19(3): 551-554.
600 DOI:10.5194/nhess-19-551-2019

601 Li, X., Dellinger, G., Erpicum, S., Chen, L., Yu, S., Guiot, L., Archambeau, P., Pirotton, M., &
602 Dewals, B. (2024). 2D and 3D Computational Modeling of Surface Flooding in Urbanized
603 Floodplains: Modeling Performance for Various Building Layouts. Water Resources
604 Research, 60(5), e2023WR035149. doi:https://doi.org/10.1029/2023WR035149

605 Li, X., Erpicum, S., Mignot, E., Archambeau, P., Pirotton, M., & Dewals, B. (2022). Laboratory
606 modelling of urban flooding. Scientific Data, 9(1), 159. doi:10.1038/s41597-022-01282-w

Li, X., Yu, S., Kitsikoudis, V., Dellinger, G., Chen, L., Erpicum, S., Guiot, L., Lai, C., & Dewals, B. (2025). 3D numerical modelling of flow exchanges between flooded streets and residential blocks during urban flooding in an idealized district. Journal of Hydrology, 133150. doi:https://doi.org/10.1016/j.jhydrol.2025.133150

Liang, C., Guan, M., 2024. Effects of urban drainage inlet layout on surface flood dynamics and discharge. Journal of Hydrology, 632: 130890. DOI:https://doi.org/10.1016/j.jhydrol.2024.130890

Lugina, F.P., Uchida, T., 2026. The effect of channel meander on flow resistance with different aspect ratio, bed roughness, and sinuosity: fixed-flatbed cases. Journal of Hydrology 666, 134864

Luo, H., Fytanidis, D.K., Schmidt, A.R., García, M.H., 2018. Comparative 1D and 3D numerical investigation of open-channel junction flows and energy losses. Advances in Water Resources, 117: 120-139. DOI:https://doi.org/10.1016/j.advwatres.2018.05.012

Luo, P., Luo, M., Li, F., Qi, X., Huo, A., Wang, Z., He, B., Takara, K., & Nover, D. (2022). Urban flood numerical simulation: Research, methods and future perspectives. Environmental Modelling & Software, 105478. doi:https://doi.org/10.1016/j.envsoft.2022.105478

Mejía-Morales, M.A., Mignot, E., Paquier, A., Proust, S., 2023. Laboratory Investigation Into the Effect of the Storage Capacity of a City Block on Unsteady Urban Flood Flows. Water Resources Research, 59(4): e2022WR032984. DOI:https://doi.org/10.1029/2022WR032984

Mejía-Morales, M.A., Mignot, E., Paquier, A., Sigaud, D., Proust, S., 2021. Impact of the porosity of an urban block on the flood risk assessment: A laboratory experiment. Journal of Hydrology, 602: 126715. DOI:https://doi.org/10.1016/j.jhydrol.2021.126715

Mejía Morales, M.A., 2022. Influence des échanges de débit entre les rues et un bloc de bâtiments durant une inondation urbaine: Expériences de laboratoire sous écoulement stable et instable. PhD thesis, Université de Lyon

Menter, F.R., 1994. Two-equation eddy-viscosity turbulence models for engineering applications. AIAA Journal 32, 1598–1605

Mignot, E., Li, X., Dewals, B., 2019. Experimental modelling of urban flooding: A review. Journal of Hydrology, 568: 334-342. DOI:https://doi.org/10.1016/j.jhydrol.2018.11.001

Ouro, P., Cea, L., Croquer, S., Dong, W., Garcia-Feal, O., Navas-Montilla, A., Rogers, B.D., Uchida, T., Juez, C., 2024. Benchmark of computational hydraulics models for open-channel flow with lateral cavities. Journal of Hydraulic Research 62, 441–460

Rosenzweig, B. R., Herreros Cantis, P., Kim, Y., Cohn, A., Grove, K., Brock, J., Yesuf, J.,

Mistry, P., Welty, C., McPhearson, T., Sauer, J., & Chang, H. (2021). The Value of Urban Flood Modeling. Earth's Future, 9(1), e2020EF001739-e002020EF001739

Saleem, M.W., Rashid, M., Haider, S., Khalid, M., Elfeki, A., 2025. Simulation of urban flooding using 3D computational fluid dynamics with turbulence model. Results in Engineering, 25: 103609. DOI:https://doi.org/10.1016/j.rineng.2024.103609

Sañudo, E., Cea, L., Puertas, J., Naves, J., Anta, J., 2024. Large-scale physical facility and experimental dataset for the validation of urban drainage models. Hydrological Processes, 38(1): e15068. DOI:https://doi.org/10.1002/hyp.15068

Shaheed, R., Mohammadian, A., Kheirkhah Gildeh, H., 2019. A comparison of standard k–ε and realizable k–ε turbulence models in curved and confluent channels. Environmental Fluid Mechanics, 19(2): 543-568. DOI:10.1007/s10652-018-9637-1

Tang, Z., Wang, P., Li, Y., Sheng, Y., Wang, B., Popovych, N., Hu, T., 2024. Contributions of climate change and urbanization to urban flood hazard changes in China's 293 major cities since 1980. Journal of Environmental Management 353, 120113

Torres, C., Borman, D., Matos, J., Neeve, D., 2022. CFD Modeling of Scale Effects on Free-Surface Flow over a Labyrinth Weir and Spillway. Journal of Hydraulic Engineering, 148(7): 04022011. DOI:10.1061/(ASCE)HY.1943-7900.0001989

Uchida, T., Fukuoka, S., 2019. Quasi-3D two-phase model for dam-break flow over movable bed based on a non-hydrostatic depth-integrated model with a dynamic rough wall law. Advances in Water Resources 129, 311–327

Viccione, G., Izzo, C., 2022. Three-dimensional CFD modelling of urban flood forces on buildings: a case study. Journal of Physics: Conference Series, 2162(1): 012020. DOI:10.1088/1742-6596/2162/1/012020

Wang, M., Fu, X., Zhang, D., Chen, F., Liu, M., Zhou, S., Su, J., Tan, S.K., 2023. Assessing urban flooding risk in response to climate change and urbanization based on shared socio-economic pathways. Science of The Total Environment 880, 163470.

Wilcox, D.C., 2008. Formulation of the k-w Turbulence Model Revisited. AIAA Journal 46, 2823–2838

Wu, Y., Han, X., Lin, P., 2024. Numerical simulation and characteristic analysis of flood intrusion into streets and buildings. Journal of Hydrology, 631: 130751. DOI:https://doi.org/10.1016/j.jhydrol.2024.130751

Xia, J., Falconer, R.A., Wang, Y., Xiao, X., 2014. New criterion for the stability of a human body in floodwaters. Journal of Hydraulic Research, 52(1): 93-104. DOI:10.1080/00221686.2013.875073

Yuan, X., Wu, M., Tian, F., Wang, X., Wang, R., 2024. Identification of influencing factors

and risk assessment of underground space flooding in the mountain city. International Journal of Disaster Risk Reduction, 113: 104807. DOI:https://doi.org/10.1016/j.ijdrr.2024.104807

Zhu, Z., Gou, L., Liu, S., Peng, D., 2023. Effect of urban neighbourhood layout on the flood intrusion rate of residential buildings and associated risk for pedestrians. Sustainable Cities and Society, 92: 104485. DOI:https://doi.org/10.1016/j.scs.2023.104485